Three-dimensional zinc oxide nanostars anchored on graphene oxide for voltammetric determination of methyl parathion

Shaktivel Manavalan[1] · Pitchaimani Veerakumar[2,3] (ID) · Shen-Ming Chen[1] · King-Chuen Lin[2,3]

Abstract

The two-step microwave method was used to synthesize zinc oxide nanostars linked to graphene oxide (GO) nanosheets. The material was used to modify a screen printed carbon electrode (SPCE) and then explored as a binder-free electrocatalyst for the electrochemical determination of methyl parathion (MP). The morphology and crystallinity of the material were characterized by various techniques. The modified SPCE shows extraordinary electrochemical performances for sensitive determination of MP. Figures of merit include (a) a wide linear dynamic range (0.03–670 μM), (b) a low detection limit (1.2 nM; at S/N = 3), (c) a comparably low working voltage (−0.69 V vs. Ag/AgCl); and (d) an excellent sensitivity (16.5 μA μM^{-1} cm^{-2}) that surpasses other modified electrodes. The sensor was successfully applied to the determination of MP, even in the presence of other common electroactive interference, in (spiked) fruits and vegetables.

Keywords Electrochemical detection · Organophosphate pesticide · Electrocatalytic activity · Cyclic voltammetry · Differential pulse voltammetry

Introduction

Graphene-based zinc oxide (ZnO) nanocomposite have been used in energy storage, detection, sensing, photocatalyst, antimicrobial, and degradation of pollutants [1, 2]. Their tunable textural properties, such as pore size, pore volume, and surface area, render a wide range of applications in materials sciences and chemistry [3], including as excellent support materials for electrochemical sensors, and photocatalysts [4, 5]. Besides, ZnO shows potential for biosensing due to their properties including biocompatibility, nontoxicity, high chemical stability, and high electrocatalytic effect. GO is one of the most attractive materials, which has excellent electron mobility of charge carriers, high specific surface area, and outstanding electrical conductivity as well as high optical transparency [6]. Further, the oxygen fuctional groups (OFGs) such as alkoxy, carboxy, and carbonyl are attached to the edges of the GO sheets to have hydrophilic properties make it an ideal candidate for fabrication of novel electrode materials for electrochemical sensing of pesticides [7–9]. ZnO was conventionally utilized as the active electrode materials in electrochemical applications because of its outstanding catalytic ability and electrical conductivity. ZnO can also provide a large surface area to increase the mass and electrons transfer during the reactions. Therefore, the main focus of this study is to identify the possibility of direct electrochemical uses of ZnO/GO nanocomposite.

Organophosphorus pesticides (OPs) play an important role in pest control in agriculture, owing to the widespread use of pesticides, and such pesticide residuals in food have become a serious public health issue [10]. Specifically, methyl parathion (MP; O,O-dimethyl-O-(4-nitrophenyl) phosphorothioate), a

✉ Pitchaimani Veerakumar
  spveerakumar@gmail.com

✉ Shen-Ming Chen
  smchen78@ms15.hinet.net

✉ King-Chuen Lin
  kclin@ntu.edu.tw

[1] Department of Chemical Engineering and Biotechnology, National Taipei University of Technology, Taipei 10608, Taiwan, Republic of China

[2] Department of Chemistry, National Taiwan University, Taipei 10617, Taiwan, Republic of China

[3] Institute of Atomic and Molecular Sciences, Academia Sinica, Taipei 10617, Taiwan, Republic of China

typical nitroaromatic OP pesticide, has been widely utilized in many countries to avoid agriculture losses caused by insect attacks. It may disrupt the cholinesterase enzyme to cause the problems of respiratory paralysis and death [11]. So far, numerous analytical methods such as, gas chromatography (GC) [12], high performance liquid chromatography (HPLC) [13], colorimetry [14], and capillary electrophoresis (CE) [15] have been widely apporached for the determination of MP. These methods are generally accurate and sensitive, although they are usually expensive, laborious, time-consuming, sometimes require tedious pretreatment procedures, and are not convenient for on-site or in-field detection [16]. Electrochemical method has been suggested to be an efficient alternative for the quantification of OPs in environmental samples, due to its advantages of time-saving, low cost, short operation time, high sensitivity, good selectivity, and real-time online detection. For instance, an electrochemical synthesis of reduced graphene oxide (ERGO) material has been exploited for the electrochemical determination of MP in the concentration range from 3.0×10^{-8} to 2×10^{-9} M with limit of detection (LOD) of ca. 8.87×10^{-10} M [17]. Besides, Yue et al. [11] established a novel sensor for MP based on monolayer of zirconium(IV) phosphonate coupled with a glassy carbon electrode (GCE) which was measured by square wave voltammetry (SWV) at around -0.28 V vs. saturated calomel electrode. They achieved the MP LOD of 0.25 ng mL^{-1} in the concentration range from 1.0 to 100 ng mL^{-1}. Nanostructured metal oxides show significant electron-transfer kinetics and have larger specific surface area; therefore, they have a larger number of adsorption sites on the surface of the working electrode and are widely applied in the detection of MP molecules. Song et al. [18] reported titanium dioxide combined with graphene (TiO$_2$/graphene) in an electrochemical sensing of MP. This method offered two ranges (0.002 ~ 5 μM and 5 ~ 100 μM) and LOD of 1.0 nM (S/N = 3) for MP. Muthumariappan et al. applied the reduced graphene oxide supported zinc oxide (RGO-ZnO) nanocomposite-modified electrode to improve the sensitivity of electrocatalytic activity toward MP detection. The electrochemical sensor exhibited a linear dependence on MP concentration ranging from 5 to 100×10^{-9} M with a LOD of 1.22×10^{-9} M (S/N = 3) [19]. In this work, the integration (or hybridization) of zinc oxide nanostars ZnONSts with GO (ZnONSt@GO) has been used as the low-cost catalyst. ZnONSt@GO nanocomposite used in electrochemical detections of MP is much more efficient than the ZnO alone. Consequently, the nanocomposite was adopted in the modified electrode for the voltammetric determination of MP.

In this study, we report the two-step microwave-assisted synthesis for fabricating ZnONSt@GO nanocomposite for electrochemical detection of MP (Scheme 1). The modified SPCE presents high sensitivity, low potential and long-term stability towards the detection of MP.

Experimental section

Chemicals and reagents

Zinc(II) nitrate hexahydrate (98%), hexamethylenetetramine (HMTA, ≥99.0%), polyvinylpyrrolidone (PVP, Mw ~ 40,000), methyl parathion (MP, PESTANAL®, analytical standard), and graphite powder (<20 μm) were purchased from Sigma-Aldrich (http://www.sigmaaldrich.com/taiwan.html) and used without further purification. Screen printed carbon electrode (SPCE) was purchased from Zensor R&D Co., Ltd. (http://www.zensor.com.tw/about/about.html). MP standard solutions were prepared by dilution of the standard solution with highly purified water to multilevels, and stored at 4 °C in the dark before use. All the other chemicals used were analytical-grade reagents without further purification. Phosphate buffer (PB) was prepared by mixing 0.1 M KH$_2$PO$_4$ and K$_2$HPO$_4$ solution to appropriate pH value. Milli-Q water was used as the solvent for all the studies.

Preparation of the zinc oxide nanostar@graphite oxide (ZnONSt@GO) nanocomposite

The experimental details about the preparation of graphene oxide (GO) processes using a modified Hummers method were previously reported [20] Typically, Zn(NO$_3$)$_2$.6H$_2$O (0.5949 g, 2.0 mmol) and PVP (100 mg) were gradually mixed under vigorous stirring into 30 mL Milli-Q water followed by ultrasonication for 45 min in a 50 mL beaker. HMTA (0.2803 g, 2 mmol) was subsequently added to the reaction mixture at room temperature, while keeping 1:1 M ratio between Zn^{2+} and HMTA. Then the resulting homogeneous white suspension of Zn(OH)$_2$ was transferred into a microwave (MW) synthesis work station (Milestone's START; power 300 W) heated at 100 °C for 60 min and then cooled at room temperature. The achieved product was centrifuged and washed with Milli-Q water for several times until the pH of the filtrate became neutral. Finally, the corresponding centrifugal products were denoted as ZnONSt and dried in a vacuum furnace at 85 °C for overnight.

For the preparation of the nanocomposite, 100 mg of GO was suspended in 20 mL of Milli-Q water and the suspension was under ultrasonication by keeping the GO/ZnONSt weight ratio (1:1). The reactant mixture was maintained at 100 °C for the microwave refluxing (microwave power 300 W) for 45 min. Finally, the MW irradiated nanocomposite was centrifuged, washed with Milli-Q water, and then vacuum-dried at 85 °C. The resultant nanocomposite was denoted as ZnONSt@GO (see Scheme 1).
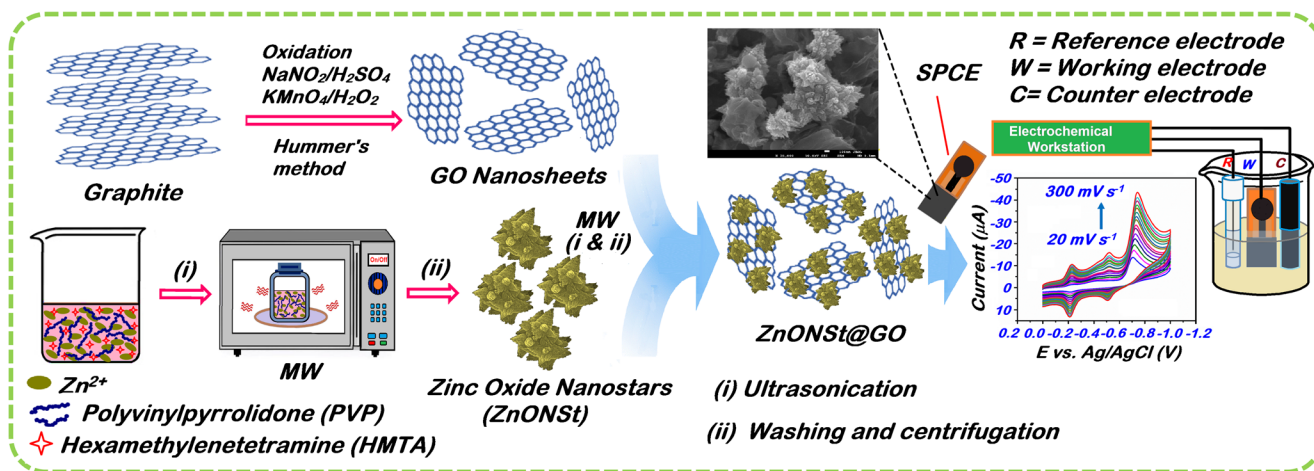
Scheme 1 Schematic representation of the preparation route and application of ZnONSt@GO nanocomposite.

Results and discussion

Powder X-ray diffraction

Figure 1a illustrates the XRD patterns of GO, ZnONSt, and ZnONSt@GO nanocomposite. A strong peak at 2θ = 10.9° in ZnONSt is characteristic of carbon peak (001) for GO sheets corresponding to d-spacing (see Fig. 1a). The relatively small peak, marked with the star (*) and seen about 2θ of 25°, corresponds to the typical (002) planes of graphene layers. This is due to the involvement of functional groups containing oxygen on the graphene/graphene oxide layers. The diffraction peaks of ZnONSt are all consistent with the hexagonal Wurtzite structure (JCPDS number 79–2205) having 2θ values of 31.4°, 34.4°, 36.5°, 47.4°, 56.6°, 62.8°, 67.8°, and 69.1° originated from the corresponding planes of (100), (002), (101), (102), (110), (103), (112), and (201), respectively. The ZnONSt@GO nanocomposite also shows the same characteristic diffraction peaks with the ZnONSt. One can notice that the characteristic diffraction peaks of ZnO in XRD pattern of nanocomposite are broader than those of neat ZnONSt. This broadening refers to the strong interaction of ZnONSt with GO nanosheets in nanocomposite structure. The particle (crystalline) size is calculated by Debye-Scherrer eq. ($D = K\lambda/(\beta \cos \theta)$; D means crystallite size, K the constant = 0.89, λ the wavelength of Cu-Kα = 0.15406 nm, β the full width at half-maximum (FWHM), θ the diffraction angle) [21]. The estimated particle size of the ZnO nanostructures is about 550 nm, which is very close to the size determined by FE-TEM images (vide-infra).

Raman analysis

The Raman spectra of ZnONSt, GO and ZnONSt@GO nanocomposite are displayed in Fig. 1b. Three dominant peaks are located at 327, 444, and 586 cm^{-1} in the ZnONSt Raman spectrum. The 329 cm^{-1} peak is generated from second-order Raman spectrum emerging from zone boundary phonons of hexagonal ZnO. The intense peak that appeared at 440 cm^{-1} is assigned to non-polar optical phonon E_2 (HI) vibration mode of ZnONSt in Wurtzite structure. Finally, the peak at 584 cm^{-1} corresponds to the E_1 (LO) mode of hexagonal ZnO, which is associated with the oxygen deficiencies [22]. On the other hand, the Raman spectrum of GO exhibit two characteristic peaks of carbonaceous materials located at ~1346 (D-band) and ~1589 cm^{-1} (G-band). The D band appears from the defects introduced by the attachment of oxygen containing functional groups (OFGs) on the graphene's basal plane, while the G band is ascribed to the first-order scattering of the E_{2g} mode [23]. The Raman spectrum of ZnONSt@GO nanocomposite shows similar characteristic peaks of G and D bands of GO in ZnONSt nanocomposite to have the D band at ~1368 cm^{-1} and the G band at ~1603 cm^{-1}. Also, the intensity ratio of the D to the G band (I_D/I_G) for GO (1.04) is higher than that for ZnONSt@GO (0.98). The I_D/I_G customarily acts as a parameter to evaluate the disorder and defect degree of various carbon materials; that is, the higher ratio of I_D/I_G accounts for the higher degree of disordering in the carbon materials. Thus, the decreased intensity ratio in the ZnONSt@GO nanocomposite reveals a decrease in the amount of defects induced by the attachment of OFGs upon microwave-assisted hydrothermal method.

Fourier transform infrared spectroscopy

Figure 1c shows the Fourier transform infrared spectrometer (FT-IR) spectra of GO, ZnONSt, and ZnONSt@GO nanocomposite. The absorption band at 527 cm^{-1} in ZnONSt is attributed to the vibration of Zn–O bonds. Three additional peaks at 1602, 1410, and 1105 cm^{-1} can be assigned to the
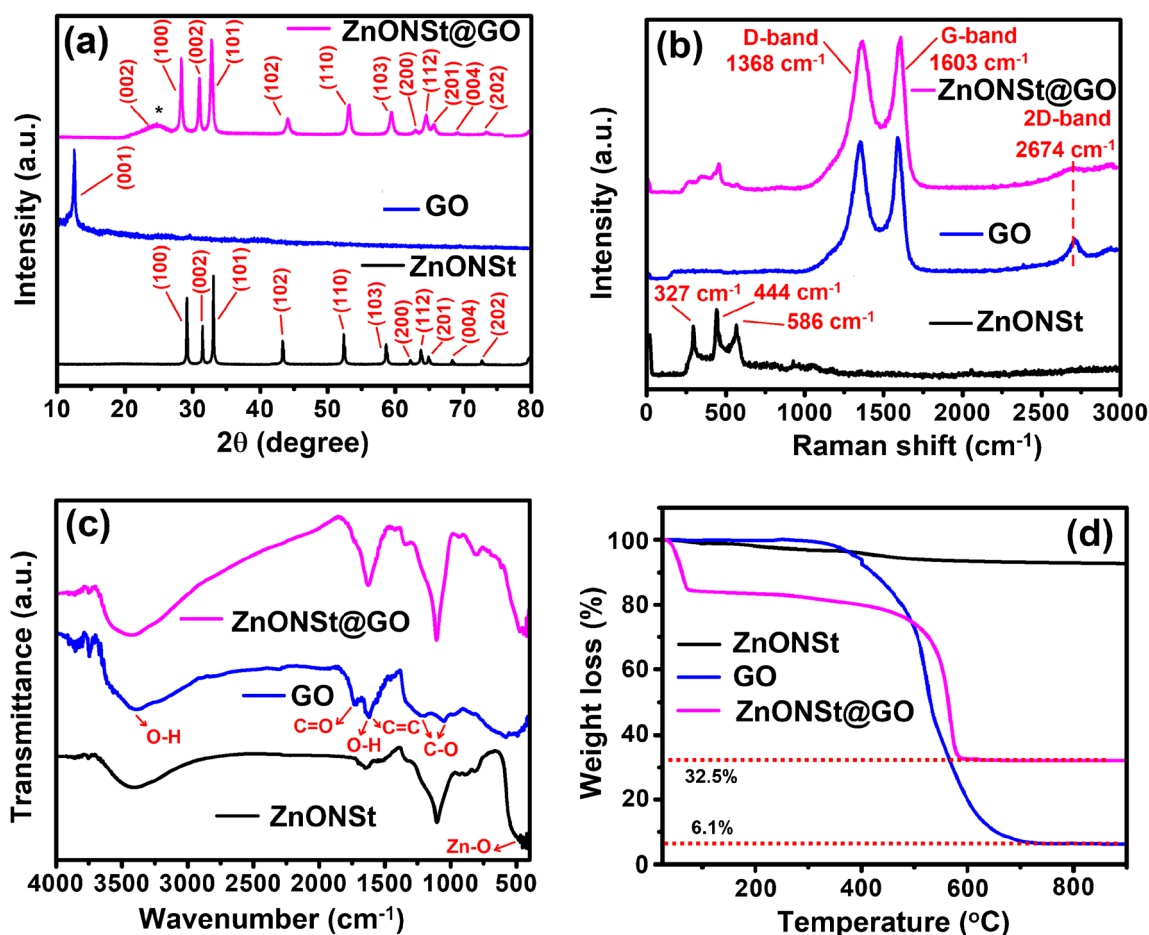
Fig. 1 (a) XRD patterns, (b) Raman spectra, (c) FT-IR spectra, and (d) TGA curves of ZnONSt, GO, and ZnONSt@GO

asymmetric stretching modes and an out-of-phase bending mode was also observed at 875 cm^{-1} [23]. The stretching vibration of surface hydroxyl groups (–OH) is confirmed by the broad absorption band at 3400 cm^{-1}, O-H bending vibration (1621 cm^{-1}), C=O stretching vibration (~1726 cm^{-1}), C-O stretching vibrations of epoxy group (1240 cm^{-1}), C-OH stretching vibrations (~1380 cm^{-1}) and C=C skeletal ring vibrations (~1627 cm^{-1}) of the GO sample [24]. Due to interactions between the ZnONSt and residual epoxy and hydroxyl functional groups of the GO, the band of ZnO was red-shifted to 470 cm^{-1} in the ZnONSt@GO nanocomposite, indicating that ZnONSt is well incorporated with GO materials.

Thermogravimetric analysis

The thermal stability of ZnONSt, GO, and ZnONSt@GO nanocomposite was analyzed using TGA at the dynamic heating rate of 10 °C min^{-1} measured in air conditions; the results are displayed in Fig. 1d. The first weight loss observed at 25–100 °C was attributed to the desorption of surface bound water molecules existing in GO of ZnONSt@GO. The abrupt weight loss in the range of ~400–600 °C may be attributed to

the pyrolysis of the labile oxygen-containing functional groups and decomposition of carbon framework from the nanocomposites [25]. The residue of GO is approximately 6.1 wt.%, while the ZnONSt@GO sample is approximately 32.5 wt.%. Therefore, the ZnO content in the nanocomposite was determined to be about 26.4 wt.%. Besides, as compared to the pristine GO, ZnONSt@GO features a lower thermal stability because of the carbon catalytic decomposition of ZnO [26].

X-ray photoelectron spectroscopy

The surface composition and element analysis for the GO and ZnONSt@GO nanocomposite were characterized by XPS. As shown in Fig. S1a (SI), the XPS scan survey spectra reveal the presence of Zn, O, and C elements. The higher-resolution XPS spectrum of Zn 2p (Fig. S1b, SI) shows two peaks of binding energy (BE) at 1022.4 and 1046.6 eV, corresponding to the electron orbits of Zn 2p$_{3/2}$ and Zn 2p$_{1/2}$, respectively [27]. The deconvoluted C 1 s XPS spectrum of ZnONSt@GO is resolved into three components as displayed in Fig. S1c, SI. The BE peaking at 284.7 eV originates from the C–C or

C=C bond, and the peaks at 285.6 and 289.5 eV are attributed to C–O and O–C=O bond, corresponding to alkoxy and carboxyl, respectively. In Fig. S1d (SI), the O 1 s profile can be fitted to two BE peaks at 530.9 and 532.8 eV, which can be attributed to the lattice oxygen in ZnO and the oxygen in C–OH and C–O–C of the ZnONSt@GO nanocomposite, respectively. These results indicate the existence of the OFGs, such as alkoxy, carboxyl, or hydroxyl on the surface of GO and anchor ZnONSt to form an integrated nanocomposite [28].

Nitrogen sorption

The N_2 sorption measurements were conducted to evaluate the BET surface areas and pore-size distributions of the ZnONSt and ZnONSt@GO samples (Fig. S2, SI). The two samples exhibit type-IV isotherm (cf. Brunauer-Emmett-Teller) with a hysterias loop. Barrett-Joyner-Halenda (BJH) pore-size distribution (inset Fig. S2, SI) demonstrated that the mesopores (3–140 nm) existed in both samples, confirming the presence of meso−/macropores. Furthermore, the ZnONSt@GO has a surface area of 34.3 m^2 g^{-1}, which is much smaller than that of GO (46.8 m^2 g^{-1}); the data are not shown. The surface areas (S_{BET}), total pore volumes (V_{Tot}), and pore sizes (D_p) of the ZnONSt and ZnONSt@GO samples are listed in Table S1, SI. The decrease in surface area of ZnONSt@GO is due to the incorporation of ZnONSt on the surface of GO sheets.

Structural analysis

The morphology and microstructure of these samples were characterized by field emission-scanning electron microscopy (FE-SEM), which is depicted in Fig. 2. An observation of the surface morphology at a high magnification of the FE-SEM image (Fig. 2a) reveals that the number of GO nanosheets possess a small number of flake-like sheets with wrinkled structures [19]. This impiles that the individual layers are stacked via van der Waals interactions of the oxygen functional groups from the basal planes and from the edges of GO. In Fig. 2b, it can be observed that the ZnONSt exhibits a star-like morphology with the average size of 625 ± 10 nm and the pedant arm of the individual nanostars reveals the crystalline nature (Fig. 2c-g), which is consistent with XRD results (vide-supra).

Figure 3a shows the FE-TEM images of ZnONSt, which has sizes of few hundred nanometers along with robust star-like shape of the microstructure. For the ZnONSt@GO nanocomposite (Fig. 3b-d), the ZnONSt are interconnected on the surface of GO and well separated from each other and distributed randomly on the surface of GO nanosheets, which is consistent with the FE-SEM and XRD results. These results also confirm the presence of star-like shape structure with an average size of >500 nm diameter as well as little surface roughening of the arm structure (see in Fig. 3b-d). In addition,

the selected area electron diffraction (SAED) reveals that the nanocomposite shows a crystalline nature (Fig. 3e). Atomic percentage and weight percentage of various elements present in the nanocomposite are evaluated based on energy dispersive X-ray analysis (EDX) and shown in Fig. 3f. The EDX analysis also shows the absence of any other type of impurity in the nanocomposite.

Energy dispersive X-ray analysis

Energy dispersive X-ray (EDX) spectrum was another important tool to examine the elemental composition of the ZnONSt@GO nanocomposite. Apparently, the elements of zinc, oxygen and carbon were reflected in EDX spectrum, which further strongly confirmed the purity of the nanocomposite. The ZnONSt@GO consisted of 56.2 wt% of C, 25.5 wt% of Zn, and 18.3 wt% of O. However, the Cu signals are due to diffuse scattering from the supporting grid. Hence, it is concluded that the synthesized ZnONSt@GO nanocomposite was high in purity with consistent particles size. According to FE-SEM/TEM and SAED results, the ZnONSt nanocomposites are mostly in the form of star-like morphology crystals, which are closely embedded on the surface of GO nanosheets.

The elemental mapping images indicate the spatial distribution of the elements (C, N, Zn and O) present in ZnONSt@GO. It is observed that the density distribution of Zn matches well with O; the coexistence of C and N confirms the loading of GO on the surface of ZnONSts (Fig. S3, SI). All of above results corroborate that hybrid ZnONSt@GO nanocomposite materials along with polycrystallized structure through the MW synthesis technique were successfully prepared.

Formation mechanism of ZnONSt nanostructure

Based on the experimental results, the formation mechanism for the ZnONSt nanostructures can be tentatively depicted in Scheme S1. Interactions between the PVP and Zn^{2+} ions are through steric and electrostatic stabilization of the amide groups of the pyrolidine rings as well as the methylene groups (Scheme S1, SI), showing that the PVP acts as a stabilizer for dissolved zinc salts. Initially, the PVP stabilizer was dissolved in an aqueous solution after adsorbed onto the surfaces of Zn^{2+} ions. When HMTA was further introduced, the ZnO nuclei comprising assembled ZnO nanostars (ZnONSt) were achieved (Fig. S2). Note that the overall reactions referred in the literature for the role of HMTA and ZnO nanostructure formation are expressed in the following,
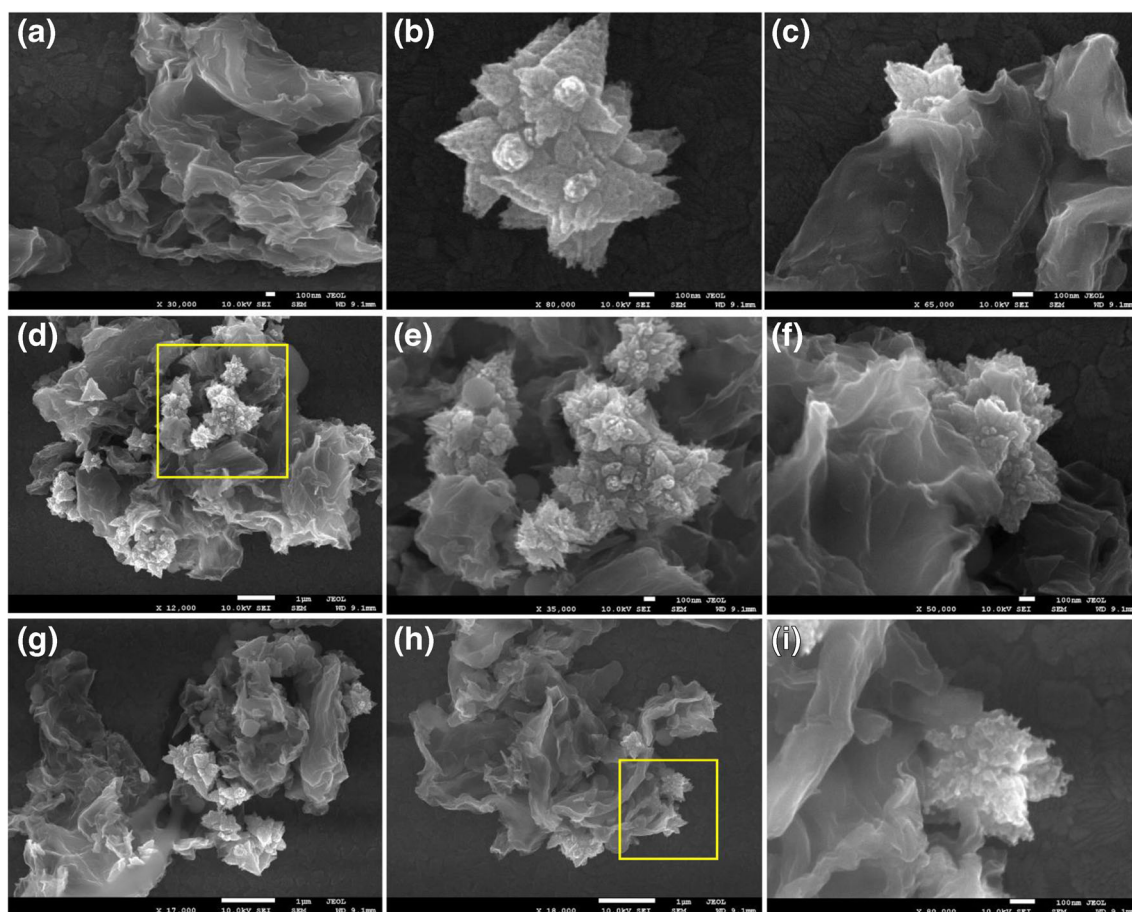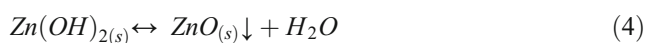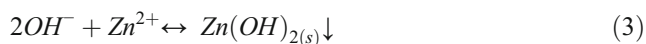
$$C_6H_{12}N_4 + 6H_2O \rightarrow 6CH_2O + 4NH_3 \quad\quad (1)$$

$$NH_3 + H_2O \leftrightarrow NH_4^+ + OH^- \quad\quad (2)$$
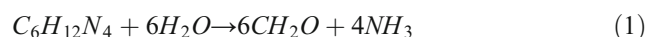
Fig. 2 Representative FE-SEM images of (**a**) GO nanosheets, (**b**) ZnONSt, and (**c-i**) ZnONSt@GO nanocomposite at different magnifications

$$2OH^- + Zn^{2+} \leftrightarrow Zn(OH)_{2(s)}\downarrow \qquad (3)$$

$$Zn(OH)_{2(s)} \leftrightarrow ZnO_{(s)}\downarrow + H_2O \qquad (4)$$

When the precursor solution is heated and maintained at 100 °C, HMTA hydrolyzes to form formaldehyde (CH$_2$O) and ammonia (NH$_3$) (eq. 1). The NH$_3$ reacts with water to produce hydroxide (OH$^-$) ions (eq. 2); therefore, HMTA provides continuous source of OH$^-$ ions gradually to make the solution under alkaline condition. Then Zn^{2+} ions combined with OH$^-$ ions to form Zn(OH)$_2$ precipitates as shown in eq. 3, which drives the crystallization of ZnO rapidly at 100 °C. As a consequence, the rod-like ZnO crystals were formed (see Fig. S4, SI) growing along one direction and almost completely nucleated [29]. In this step, during the following MW heating process, the rod-like ZnO particles gradually transform into ZnO nanostars via Ostwald ripening (eq. 4). In other words, to reduce the surface energy these ZnO rods rapidly assemble into ZnO nanostars. In addition, alkaline ions have been proved to have structural-direction effect and PVP are used to control the shape and size of metal oxide.

Electrochemical studies

Generally, electrochemical impedance spectroscopy (EIS) techniques was conducted to understand the conductivity, and charge transport in the material/electrolyte interface of the electrodes. The electrocatalytic performance of the ZnONSt@GO/SPCE was investigated by EIS using 5.0 mM [Fe(CN)$_6$]$^{3-/4-}$ with 0.1 M KCl as the supporting electrolyte versus Ag/AgCl. Figure 4a shows the Nyquist plots for the bare SPCE, ZnONSt, GO, and ZnONSt@GO/SPCE electrodes. All these plots display a semicircle in the high-frequency region and a straight line in the low-frequency region. The Warburg resistance is confined to the low-frequency range of the straight line, which arises from the frequency dependence of electron transfer and diffusion from the electrolyte to the electrode surfaces. The very high frequency range denoted in the arc (semicircle part) corresponded to the limiting stage of charge transfer, arising from the double-layer capacitance in parallel with the charge transfer resistance (R_{ct}) at the contact interface between the electrode and electrolyte solution. The R_{ct} value can be directly measured from the Nyquist plots as the semicircular arc diameter. The R_{ct} for
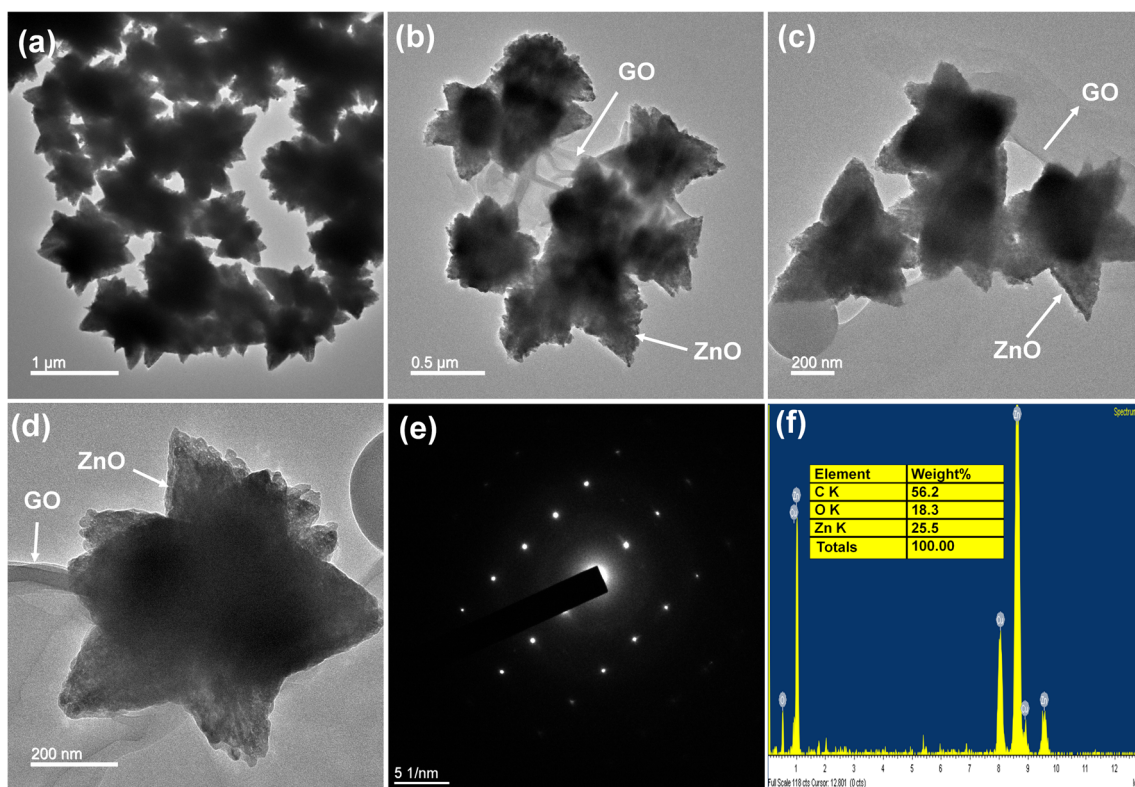
Fig. 3 FE-TEM images: (**a**) ZnONSt, (**b-d**) ZnONSt@GO nanocomposite, (**e,f**) the corresponding SEAD and EDX spectrum

the ZnONSt@GO/SPCE is 48.18 Ω, which is substantially smaller than those of pristine ZnONSt (291.81 Ω) and GO (202.01 Ω) electrodes, suggesting the superior conductivity of the ZnONSt@GO/SPCE. It also indicated that the incorporation of ZnONSt into the GO nanosheets results in an improved electron charge transfer performance for the electrode. Clearly, the EIS profiles of ZnONSt@GO nanocomposite is higher than corresponding activity of both ZnONSt and GO. A small well-defined semicircle at high frequencies is achieved at the ZnONSt-modified SPCE, signifying a better ionic conductivity nature than GO. In addition, ZnONSt@GO electrode presented low resistivity than ZnONSt, suggesting that the GO nanosheets structure decreased the resistance of electrochemical action, promoted electron transport and subsequently reduced the corresponding energy consumption. In other words, the lower charge-transfer resistance with higher electronic conductivity behavior was observed at ZnONSt@GO/SPCE. As a result, this nanocomposite reveals a good interaction between GO nanosheets and ZnONSt. Cyclic voltammetry (CV) is a viable electrochemical technique which is used to measure the electrochemical properties of an analyte or system. The CV profiles of bare SPCE, ZnONSt, GO, and ZnONSt@GO/SPCEs were carried out at a scan rate of 50 mV s^{-1} using $[Fe(CN)_6]^{3-/4-}$ as a redox probe, as presented in Fig. S5, SI.

Electrochemical determination of methyl parathion (MP)

The electrocatalytic behavior of the bare SPCE, ZnONSt, GO, and ZnONSt@GO SPCEs were preliminarily evaluated on a CV technique as depicted in Fig. 4b. The CV curves of different electrode were measured in 50 μM concentration of MP with the scan rate of 50 mV s^{-1} in N$_2$-saturated PB (pH 7.0). It can be seen that the bare SPCE provides a very little current response (−0.78 μA) to the addition of MP, thus indicating that more available defective active sites are unfavorable to transfer electrons. Similarly, the ZnONSt/SPCE weakly exhibited an inferior current response (−4.766 μA) at the over potential range and no corresponding redox peak of MP was observed. It indicates that ZnONSt/SPCE with insufficient active electrode surface may not improve the voltammetry response for MP. Although the GO/SPCE exhibited a better current response (−8.269 μA) of MP, but there was no clear corresponding redox behavior was noticed. This implies that the GO/SPCE makes improper pathway for the electron diffusion of MP. While comparing these electrodes, the ZnONSt@GO/SPCE exhibits a superior current response (−17.696 μA) with the typical corresponding redox behavior of MP. Accordingly, the ZnONSt@GO/SPCE has a superior improved conductivity to increase current response for MP more than those of pure ZnONSt and GO. This indicated that
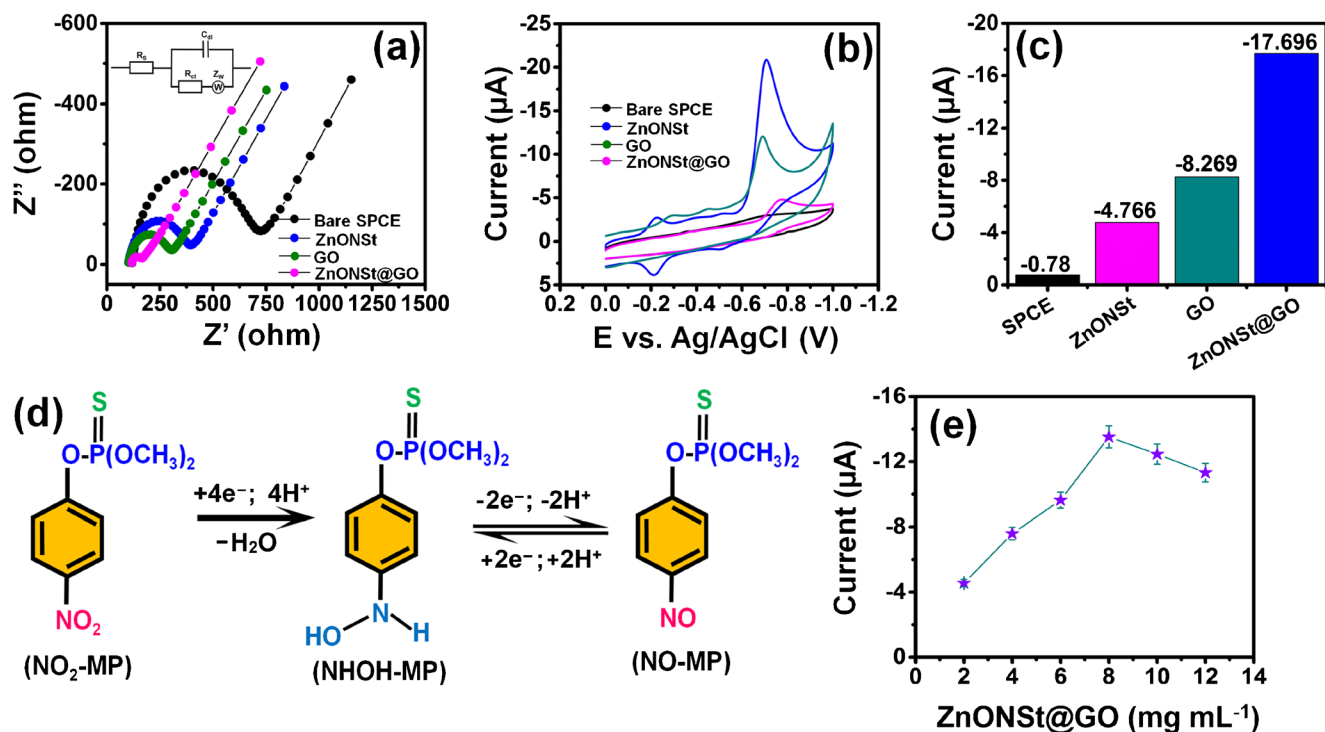
Fig. 4 (a) Electrochemical impedance spectra (Nyquist plots) recorded 5.0 mM $[Fe(CN)_6]^{3-/4-}$ containing 0.1 M KCl solution, (b) CV curves of bare SPCE, ZnONSt, GO, and ZnONSt@GO-modified SPCE in 50 μM MP measured at scan rate of 50 mV s^{-1}, (c) the corresponding peak current responses for MP over various modified electrodes, (d) schematic illustration of electrochemical mechanism of MP over the ZnONSt@GO nanocomposite, and (e) corresponding plot of electrode material concentration versus current response under N_2-saturated PB (pH 7.0) electrolyte

the addition of ZnONSt enhanced the electrocatalytic performance of GO, which contributed to the synergistic effect of the ZnONSt@GO/SPCE. On the other hand, GO serves as an interfical network to the ZnONSt in the composite, which improved the catalytic active sites for the adsorption of MP molecules. The plot of irreversible reduction peak current versus various modified electrodes is shown in Fig. 4c. The strong peak found at the potential −0.707 V is ascribed to nitro-MP (NO_2-MP) which reacted irreversibly into hydroxylamine-MP (NHOH-MP). Also, the respective redox behavior was attributed to conversion of nitroso-MP (NO-MP) reversibly into HA-MP as shown in Fig. 4d [30].

To investigate the effect of the ZnONSt@GO concentration cast onto the modified SPCE, we performed various concentration such as 2, 4, 6, 8, 10, and 12 mg mL^{-1} of ZnONSt@GO through the presence of MP (50 μM) in N_2-saturated PB (pH 7.0) at scan rate of 50 mV s^{-1}. As displayed in Fig. 4e, the reduction current response gradually rises with nanocomposite concentration from 2 to 8 mg mL^{-1}. Upon increasing concentration of ZnONSt@GO above ~8 mg mL^{-1}, the reduction current response decreases gradually and then becomes saturated; this fact indicates that the higher concentration of ZnONSt@GO made a thick film on the electrode surface that might resist the diffusion of MP.

Hence, the ZnONSt@GO is optimized at 8 mg mL^{-1} for the following electrochemical experiments.

Following a similar strategy, the electrochemical experiments were performed at different pH electrolyte so as to examine the effect of pH on the adsorption abilities of ZnONSt@GO/SPCE for the MP. Figure 5a displays the CV curves in the presence of 50 μM of MP in N_2-saturated PB and the pH range varied from 3.0–11.0 of the electrolyte at a scan rate of 50 mV s^{-1}. The irreversible reduction peak current gradually increases with increasing pH value, whilst the irreversible reduction peak current decreased with increasing pH value from 7.0–11.0. The maximum reduction peak current was observed at pH of 7.0 on the ZnONSt@GO/SPCE. The result indicates that electro-reduction of MP is mediated under pH 7.0 conditions. Hence, the pH value of 7.0 was adopted to be an optimal condition value for the further experiments. Figure 5b reveals the plot of pH (3.0–11.0) against the irreversible reduction of MP peak potential (E_{pc}) and peak current (I_{pc}) at the ZnONSt@GO/SPCE. A linearity was attained between the irreversible reduction of MP peak potential and pH (3.0–11.0) with linear regression of E_{pc} (V) = −0.0391 (± 0.0010) pH - 0.4879 (± 0.0068) and coeffecient of R^2 = 0.9977 (± 0.0016) which is almost near to the typical value of Nernst equation (−0.0592pH). This indicates that the

Fig. 5 (**a**) CV curves of 50 μM MP was recorded at scan rate of 50 mV s^{-1} as function of pH at ZnONSt@GO/SPCE under N$_2$-saturated PB at varied pH from 3.0–11.0, (**b**) the plot of pH (3.0–11.0) against the irreversible reduction of MP peak current (I_{pc}) and peak potential (E_{pc}) at the ZnONSt@GO/SPCE, (**c**) CV curves of the ZnONSt@GO/SPCE in N$_2$-saturated PB (pH 7.0) containing 50 μM MP at varied scan rates (20–300 mV s^{-1}), and (**d**) corresponding correlations between the I_{pc} versus scan rates at square root
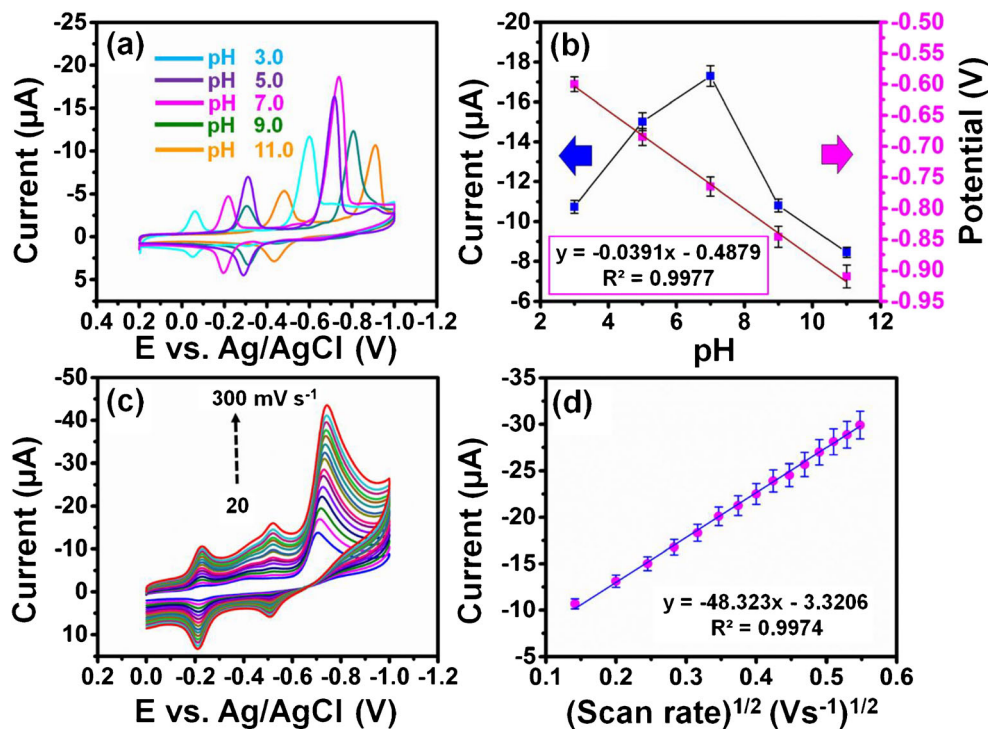
number of electrons and protons are equally transferred through the electro-reduction and oxidation of MP at ZnONSt@GO/SPCE.

Figure 5c shows that the CV curves of MP (50 μM) were measured at different scan rates from 20 to 300 mV s^{-1} over the ZnONSt@GO/SPCE in N$_2$-saturated PB (pH 7.0). As the scan rate increased from 20 to 300 mV s^{-1}, the irreversible reduction peak current and area under the CV curve increased, and the corresponding electrode still maintained its CV shape even at an increasing scan rate, which indicates the excellent capability of the electrode. In addition, the shift of irreversible reduction peaks to more right is attributed to the electric polarization when increasing the scan rate. The correlation between irreversible reduction peak current and the scan rates at square root was plotted in Fig. 5d. It shows a linear coefficient (R^2) of 0.9974 ($\pm$ 0.0008) and a regression equation of I_{pc} (μA) $= -48.323$ ($\pm$ 0.509) $\nu^{1/2}$ (mV s^{-1}) - 3.3206 ($\pm$ 0.1660), indicating that the ZnONSt@GO nanocomposite is a reliable activity-reporting material for electrochemical reduction of MP with a typical diffusion controlled process (Fig. 5d). In addition, the E_{pc} changed linearly with the natural logarithm of scan rate (ln ν) yielding a linear regression expressed as E_{pc} (mV) $= 0.0165$ ($\pm$ 0.0002) ln ν - 0.7622 ($\pm$ 0.0004) at varied scan rates (20–300 mV s^{-1}) with a coefficient (R^2) of 0.9974 ($\pm$ 0.0023), as shown in Fig. 5d.

In order to explore the heterogeneous electron rate kinetics (K_s) of MP, it can be calculated by using eq. 5 [31, 32],

$$K_s = 2.415\exp\left(\frac{-0.02F}{RT}\right)D^{1/2}\left(E_p - E_{p/2}\right)^{-1/2}V^{1/2} \qquad (5)$$

where E_p is the peak potential, $E_{p/2}$ is the potential at which the current equals a half of the peak current, and the other symbols are in their usual meanings. From this equation, K_s was calculated to be 6.01×10^{-3} cm s^{-1}.

Figure 6a depicts the amperometric response of the modified SPCE in N$_2$-saturated PB (pH 7.0) with and without the addition of MP at the potential of -0.8 V. It is also worth to notice that the current responses were constantly enhanced with increasing the concentration of MP, as shown in Fig. 6b. This result indicates the facial electron transfer occurred in an electrocatalytic reduction of MP on the SPCE. According to the Cottrell equation given in eq. 6 [33], a plot of I_p as a function of $t^{1/2}$ for each concentration of MP (Fig. 6c) yields the diffusion coefficient of MP,

$$I_p = nFAC_bD^{1/2}\pi^{1/2}t^{1/2} \qquad (6)$$

where I_p denotes the current (in A), n is the number of electrons, $F = 96{,}485$ C mol^{-1} is the Faraday constant, A is the geometric surface area of the electrode (cm^2), C_b represents the bulk concentration of the analyte (mol L^{-1}), D is the diffusion coefficient (cm^2 s^{-1}), and t is the time (s). Accordingly,

Fig. 6 (**a**) Amperometric response of the ZnONSt@GO/SPCE with and without addition of MP; (**b**) at different concentrations of MP (10–50 μM), (**c**) plots of current versus time$^{1/2}$; and (**d**) corresponding calibration plot of slope versus MP concentration. All measurements were conducted in N$_2$-saturated PB (pH 7.0)
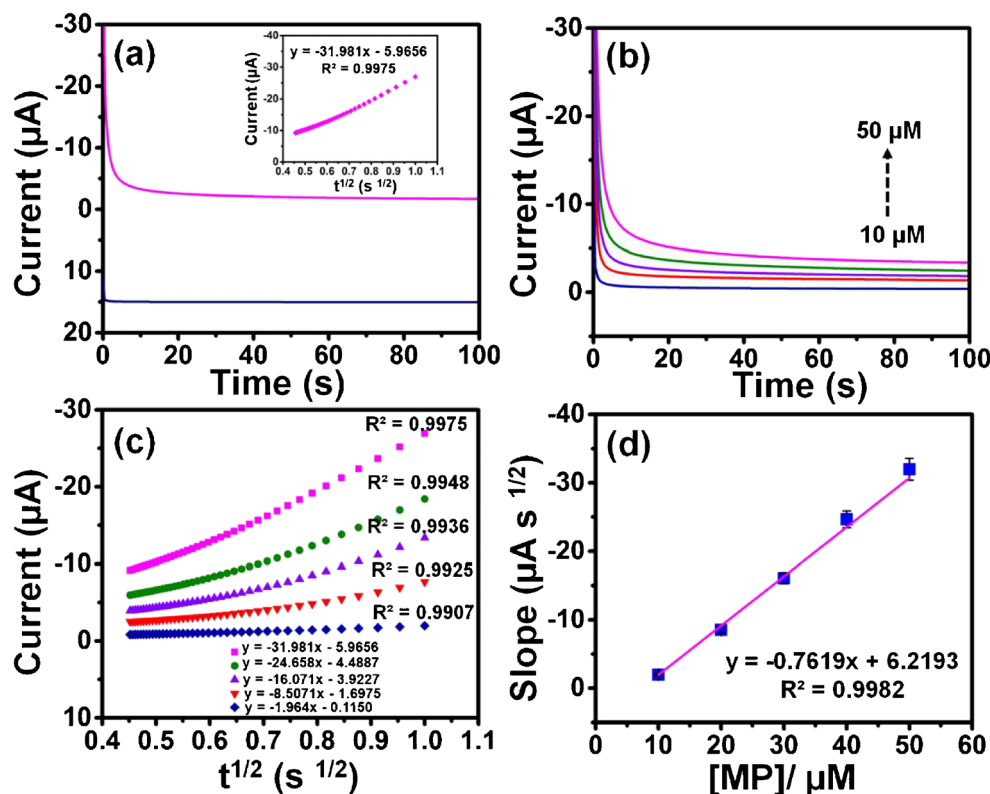
the value of $D = 2.15 \times 10^{-8}$ cm^2 s^{-1} for MP is determined from the slope in Fig. 6d.

Stability and reproducibility

Figure 7a shows DPV curves of the ZnONSt@GO/SPCE in 0.1 M PB (pH 7.0) with different concentrations of MP at a scan rate of 50 mV s^{-1}. The reduction peak current significantly increased with the successive addition of MP from the concentrations of 0.03–669.65 μM, indicating the rapid electro-reduction of MP at ZnONSt@GO/SPCE. In addition, the corresponding linear regression can be represented as I_{pc} (μA) = −0.1611 μM (± 0.0077) - 12.239 (± 0.3213) with the coefficient R^2 of 0.9907 (± 0.0219), as shown in Fig. 7b. The sensitivity and LOD were estimated to be 16.5237 μA μM^{-1} cm^{-2} and 1.23 nM based on the typical standard formula (LOD = 3(SD/slope)). Furthermore, the limit of quantification (LOQ) was calculated to be 8.61 nM by using the standard formula of LOQ = 10(SD/slope). The analytical sensing performance vaules of this fabricted sensor was compared with those MP sensors reported previously and the results are summarized in Table S2, SI. These findings demonstrate that the SPCE showed an excellent electrocatalytic activity, good linear range, and lower LOD toward the reduction of MP.

Prior to the reproducibility of this sensor, the experiments were performed by 5 different electrodes with a constant presence of 50 μM of MP containing N$_2$-saturated PB (pH 7.0). The results are depicted in supplementary Fig. S6a, SI; all electrodes show negligible variation in the current response with relative standard deviation (RSD) of −4.30%. The repeatability of the sensor was performed using single electrode for seven repeatability measurements of MP (50 μM). The result shows decrease in the current response with RSD of −3.75%; however, the decearse of current reponse between first and seventh measurement might be due to handling error and saturation in electrode surface (Fig. S6b, SI). Furthermore, the electrode storage stability was evaluated by measuring the current response for 50 μM of MP at the continuous measurement for 4 weeks (Fig. S6c, SI). After each measurement, the modified electrode was kept in PB (pH 7.0) at refrigerator (4 °C). The modified electrode showed decrease in their current response for each day measurement till the 4th weeks and exhibited 85% of its initial current response. Compare to other reported modified electrode [34], our proposed method shows comparable or better electrode stability towards MP. The good results of reproducibility, repeatability, and stability studies indicated that the SPCE is obviously suitable for analytical application.

Interference studies

The interference experiments toward 10-fold addition of fenitrothion (FT), ethyl parathaion (EP), thiamethoxam (TMX), imidacloprid (IMD), catechol (CT), hydroquinone (HQ),

Fig. 7 (**a**) DPV response of the ZnONSt@GO/SPCE under consecutive addition of MP within total dosage range of 0.03–669.65 μM, (**b**) corresponding calibration plot of response peak current (μA) versus MP concentration (μM), (**c**) DPV response of ZnONSt@GO/SPCE towards 10 μM of MP after adding 10-fold concentration of interfering species such as FT, EP, TMX, IMD, CT, HQ, RC, TA, and NaCl and, (**d**) Histogram of peak current (μA) versus MP in the presence of various interfering species. All measurements were conducted in N_2-saturated PB (pH = 7.0) at a scan rate of 50 mV s^{-1}
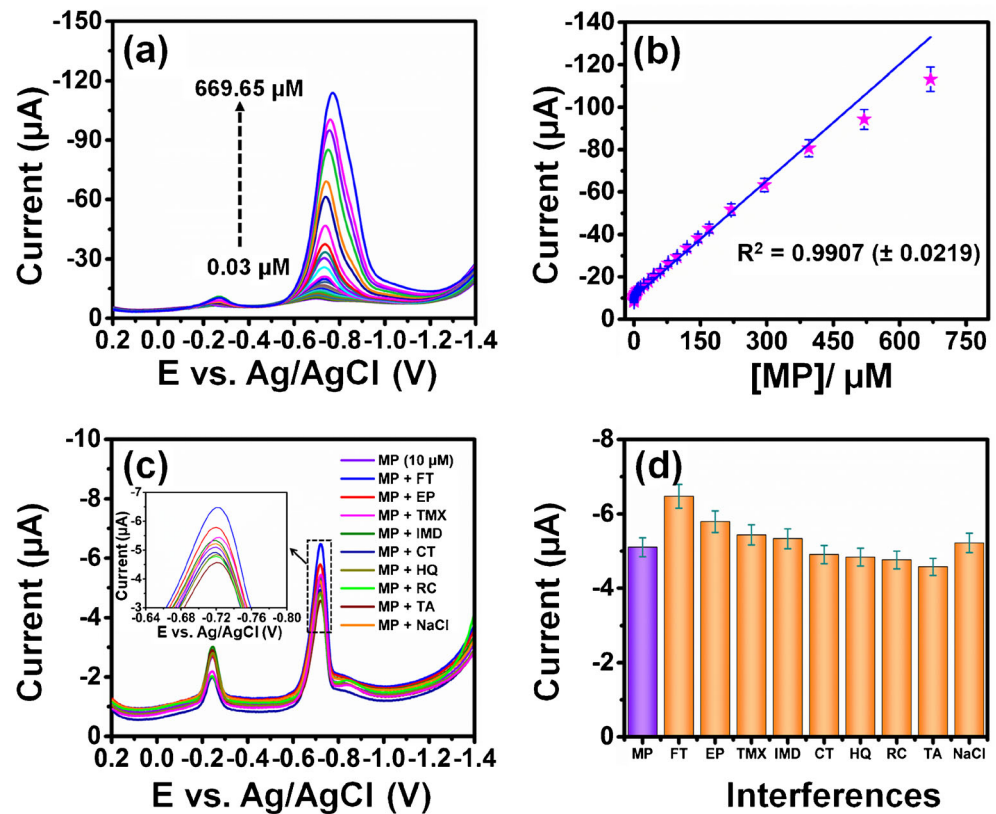
resorcinol (RC), tannic acid (TA) and NaCl have been investigated together with MP (10 μM) at ZnONSt@GO/SPCE, as displayed in Fig. 7c. Clearly, even when the 10-fold concentration of interfering species was added to MP, the current response is still satisfactory.

Real sample analysis

For practical application, modified SPCE was used to detect fruits and vegetables such as apple, broccoflower, and collard greens for the MP detection. MP is an OPs pesticide as well as

Table 1 Determination of MP in fruit and green vegetables at the ZnONSt@GO/SPCE by DPV

samples	spiked (μM)	found (μM)		recovery (%)	recovery (%)
		proposed method[a]	HPLC method[b]		
apple	unspiked	0.00	0.00	–	–
	2.0	1.97	1.98	98.50	99.00
	5.0	4.98	4.99	98.00	99.50
broccoflower	unspiked	0.00	0.00	–	–
	2.0	1.98	1.99	98.00	99.50
	5.0	4.97	4.99	98.50	99.50
collard greens	unspiked	0.00	0.00	–	–
	2.0	1.98	1.99	98.00	99.50
	5.0	4.98	4.99	98.00	99.50

[a] Proposed electrochemical method. [b] HPLC method; all measurements are an average of $n = 3$

insecticide to kill insects which affect the growth of plants. So, it has been utilized extensively by agricultural cultivation. However, MP is banned nearly in all countries, while illegal use of MP is still suspected. Firstly, the extract of apple, broccoflower and collard greens were collected from slicing followed by soaked in PB (0.1 M, pH 7.0) and squeezed to get extract. To the extract of apple, broccoflower, and collard greens sample, a known concentration of MP was added and examined by DPV under the same experimental conditions of Fig. 7d. For comparision, independent measurements using HPLC method were conducted under otherwise the same conditions. The added, found, and recoveries are summarized and tabulated in Table 1. This clearly evidences that the ZnONSt@GO/SPCE is well suitable for the electrochemical determination of MP in all the fruits and vegetables.

Conclusion

In summary, the ZnONSt@GO nanocomposite was successfully demonstrated by two-step microwave synthesis route, which showed an excellent electrochemical sensing performance of MP. Based on the high conducitivity of graphene oxide, the electrocatalytic activities of ZnONst was greatly improved. The performance of the modified SPCE was found to have superior electro-reduction of MP, showing desirable wide-linear dynamic range, a very lower detection limit, and selectivity. The feasibility of the system was demonstrated by the detection of target analytes in spiked apple, broccol and collar green samples. The drawback is that in the presence of interferent species, selectivity of target analytes has not been fully recognized. By increasing the large concentration of interfering species, our proposed method will interfere, suggesting that in individual presence a variety of analytes can be detected with this nanocomposite. However, the ZnONSt@GO nanocomposite fabrictaed electrodes can further improve the electrochemical efficiency of sensing hazardous samples. Further research on other useful applications of this nanocomposite is under progress.

Compliance with ethical standards

Conflict of interest The author(s) declare that they have no competing interests.

References

1. Saranya M, Ramachandran R, Wang F (2016) Graphene-zinc oxide (G-ZnO) nanocomposite for electrochemical supercapacitor applications. J Sci Adv Mater Dev 1:454–460. https://doi.org/10.1016/j.jsamd.2016.10.001

2. Archana S, Kumar KY, Jayanna BK, Olivera S, Anand A, Prashanth MK, Muralidhara HB (2018) Versatile graphene oxide decorated by star shaped zinc oxide nanocomposites with superior adsorption capacity and antimicrobial activity. J Sci Adv Mater Dev 3:167–174. https://doi.org/10.1016/j.jsamd.2018.02.002

3. Jilani SM, Banerji P (2014) Graphene oxide–zinc oxide nanocomposite as channel layer for field effect transistors: effect of ZnO loading on field effect transport. ACS Appl Mater Interfaces 6:16941–16948. https://doi.org/10.1021/am504501n

4. Beitollahi H, Nejad FG (2016) Graphene oxide/ZnO nano composite for sensitive and selective electrochemical sensing of levodopa and tyrosine using modified graphite screen printed electrode. Electroanalysis 28:2237–2244. https://doi.org/10.1002/elan.201600143

5. Durmus Z, Kurt BZ, Durmus (2019) A. Synthesis and characterization of graphene oxide/zinc oxide (GO/ZnO) nanocomposite and its utilization for photocatalytic degradation of basic fuchsin dye. Chem Select 4:271–278. https://doi.org/10.1002/slct.201803635

6. Wilson NR, Pandey PA, Beanland R, Young RJ, Kinloch IA, Gong L, Liu Z, Suenaga K, Rourke JP, York SJ, Sloan J (2009) Graphene oxide: structural analysis and application as a highly transparent support for electron microscopy. ACS Nano 3:2547–2556. https://doi.org/10.1021/nn900694t

7. Gao N, He C, Ma M, Cai Z, Zhou Y, Chang G, Wang X, He Y (2019) Electrochemical co-deposition synthesis of Au-ZrO$_2$-graphene nanocomposite for a nonenzymatic methyl parathion sensor. Anal Chim Acta 1072:25–34. https://doi.org/10.1016/j.aca.2019.04.043

8. Yang Y, Asiri AM, Du D, Lin Y (2014) Acetylcholinesterase biosensor based on a gold nanoparticle-polypyrrole-reduced graphene oxide nanocomposite modified electrode for the amperometric detection of organophosphorus pesticides. Analyst 139:3055–3060. https://doi.org/10.1039/C4AN00068D

9. Li Y, Xu M, Li P, Dong J, Ai (2014) Nonenzymatic sensing of methyl parathion based on graphene/gadolinium Prussian blue analogue nanocomposite modified glassy carbon electrode. Anal Methods 6:2157–2162. https://doi.org/10.1039/C3AY41820K

10. Hassan AHA, Moura SL, Ali FHM, Moselhy WA, Sotomayor MPT, Pividori MI (2018) Electrochemical sensing of methyl parathion on magnetic molecularly imprinted polymer. Biosens Bioelectron 118:181–187. https://doi.org/10.1016/j.bios.2018.06.052

11. Yue Y, Jiang L, Li Z, Yuan J, Shi H, Feng S (2019) A glassy carbon electrode modified with a monolayer of zirconium(IV) phosphonate for sensing of methyl-parathion by square wave voltammetry. Microchim Acta 186:433. https://doi.org/10.1007/s00604-019-3493-7

12. Filho AM, dos Santos FN, de Paula PA (2010) Development, validation and application of a methodology based on solid-phase micro extraction followed by gas chromatography coupled to mass spectrometry (SPME/GC–MS) for the determination of pesticide residues in mangoes. Talanta 81:346–354. https://doi.org/10.1016/j.talanta.2009.12.008

13. Wu CX, Liu HM, Liu WH, Wu QH, Wang C, Wang Z (2010) Determination of organophosphorus pesticides in environmental water samples by dispersive liquid-liquid microextraction with solidification of floating organic droplet followed by high-performance liquid chromatography. Anal Bioanal Chem 397:2543–2549. https://doi.org/10.1007/s00216-010-3790-9

14. Anh DH, Cheunrungsikarn K, Wichitwechkarn J, Surareungchai W (2011) A colorimetric assay for determination of methyl parathion using recombinant methyl parathion hydrolase. Biotechnol J 6:565–571. https://doi.org/10.1002/biot.201000348

15. Geng F, Ding J, Jia C, Ding B, Qin W (2015) A potentiometric biosensing system based on an isolated degrading bacterium Klebsiella sp. MP-6 for the determination of methyl parathion. RSC Adv 5:34475–34480. https://doi.org/10.1039/C5RA00263J

16. Xue XD, Wei Q, Wu D, Li H, Zhang Y, Feng R, Du B (2014) Determination of methyl parathion by a molecularly imprinted sensor based on nitrogen doped graphene sheets. Electrochim Acta 116:366–371. https://doi.org/10.1016/j.electacta.2013.11.075

17. Jeyapragasam T, Saraswathi R, Chen SM, Lou BS (2013) Detection of methyl parathion at an electrochemically reduced graphene oxide (ERGO) modified electrode. Int J Electrochem Sci 8(9):12353–12366

18. Song B, Cao W, Wang Y (2016) A methyl parathion electrochemical sensor based on Nano-TiO$_2$, graphene composite film modified electrode. Fuller Nanotub Car N 24(7):435–440. https://doi.org/10.1080/1536383X.2016.1174696

19. Muthumariappan S, Vedhi C (2017) Nonenzymatic sensing of methyl parathion based on RGO-ZnO nanocomposite modified glassy carbon electrode. IOSR J Appl Chem 10:55–64. https://doi.org/10.9790/5736-1009035564

20. Veerakumar P, Tharini J, Ramakrishnan M, Panneer Muthuselvam I, Lin KC (2017) Graphene oxide nanosheets as an efficient and reusable sorbents for eosin yellow dye removal from aqueous solutions. ChemistrySelect 2:3598–3607. https://doi.org/10.1002/slct.201700281

21. Bindu P, Thomas S (2014) Estimation of lattice strain in ZnO nanoparticles: X-ray peak profile analysis. J Theor Appl Phys 8:123–134. https://doi.org/10.1007/s40094-014-0141-9

22. Abdolhosseinzadeh S, Asgharzadeh H, Sadighikia S, Khataee A (2016) UV-assisted synthesis of reduced graphene oxide–ZnO nanorod composites immobilized on Zn foil with enhanced photocatalytic performance. Res Chem Intermed 42:4479–4496. https://doi.org/10.1007/s11164-015-2291-z

23. Costenaro D, Carniato F, Gatti G, Bisio C, Marchese L (2011) On the physico-chemical properties of ZnO nanosheets modified with luminescent CdTe nanocrystals. J Phys Chem C 115:25257–25265. https://doi.org/10.1021/jp209267s

24. Wang Y, Liu J, Liu L, Sun DD (2012) Enhancing stability and photocatalytic activity of ZnO nanoparticles by surface modification of graphene oxide. J Nanosci Nanotech 12:1–7. https://doi.org/10.1166/jnn.2012.6174

25. Navarro BC, Coronado E, Martí Gastaldo C, Sánchez Royo JF, Gómez Gómez M (2012) Influence of the pH on the synthesis of reduced graphene oxide under hydrothermal conditions. Nanoscale 4: 3977–3982. https://doi.org/10.1039/C2NR30605K

26. Wang J, Tsuzuki T, Tang B, Hou X, Sun L, Wang X (2012) Reduced graphene oxide/ZnO composite: reusable adsorbent for pollutant management. ACS Appl Mater Interfaces 4:3084–3090. https://doi.org/10.1021/am300445f

27. Ahmad M, Ahmed E, Hong ZL, Xu JF, Khalid NR, Elhissi A, Ahmed WA (2013) Facile one-step approach to synthesizing ZnO/graphene composites for enhanced degradation of methylene blue under visible light. Appl Surf Sci 274:273–281. https://doi.org/10.1016/j.apsusc.2013.03.035

28. Kwong TL, Yung KF (2015) Surfactant-free microwave-assisted synthesis of Fe-doped ZnO nanostars as photocatalyst for degradation of tropaeolin O in water under visible light. J Nanomater: 190747. https://doi.org/10.1155/2015/190747

29. Strano V, Urso RG, Scuderi M, Iwu KO, Simone F, Ciliberto E, Spinella C, Mirabella S (2014) Double role of HMTA in ZnO nanorods grown by chemical bath deposition. J Phys Chem C 118: 28189–28195. https://doi.org/10.1021/jp507496a

30. Ma JC, Zhang WD (2011) Gold nanoparticle-coated multiwall carbon nanotube modified electrode for electrochemical determination of methyl parathion. Microchim Acta 175:309–314. https://doi.org/10.1007/s00604-011-0681-5

31. Rajkumar C, Veerakumar P, Chen SM, Thirumalraj B, Lin KC (2018) Ultrathin sulfur-doped graphitic carbon nitride nanosheets as metal-free catalyst for electrochemical sensing and catalytic rmoval of 4-nitrophenol. ACS Sustain Chem Eng 6:16021–16031. https://doi.org/10.1021/acssuschemeng.8b02041

32. Velasco J (1997) Determination of standard rate constants for electrochemical irreversible processes from linear sweep voltammograms. Electroanalysis 9:880–882. https://doi.org/10.1002/elan.1140091116

33. Mejri A, Mars A, Elfil H, Hamzaoui AH (2019) Reduced graphene oxide nanosheets modified with nickel disulphide and curcumin nanoparticles for non-enzymatic electrochemical sensing of methyl parathion and 4-nitrophenol. Microchim Acta 186:704. https://doi.org/10.1007/s00604-019-3853-3

34. Pan D, Ma S, Bo X, Guo L (2011) Electrochemical behavior of methyl parathion and its sensitive determination at a glassy carbon electrode modified with ordered mesoporous carbon. Microchim Acta 173:215–221. https://doi.org/10.1007/s00604-011-0551-1